

Active Ornstein-Uhlenbeck Model for Bacterial Heat Engines

Roland Wiese,^{1,*} Klaus Kroy,¹ and Viktor Holubec^{2,†}

¹*Institute for Theoretical Physics, Leipzig University, 04103 Leipzig, Germany*

²*Faculty of Mathematics and Physics, Charles University, CZ-180 00 Prague, Czech Republic*

(Dated: July 1, 2024)

We use Brownian dynamics simulations to study a model of a cyclic bacterial heat engine based on a harmonically confined colloidal probe particle in a bath formed by active Brownian particles. For intermediate activities, active noise experienced by large enough probes becomes Gaussian with exponential autocorrelation function. We show that, in this experimentally pertinent regime, the probability densities for stochastic work, heat, and efficiency are well represented by those of an effective active Ornstein-Uhlenbeck particle (AOUP). Due to the probe's fast relaxation in the potential in typical experimental implementations, good agreement can prevail even when the noise autocorrelation function develops non-exponential tails. Our results show that the AOUP provides a convenient and accurate, analytically tractable effective model to mimic and analyze experimental bacterial heat engines, especially when operating with comparatively large probes and stiff traps.

I. INTRODUCTION

Recent developments in micro-manipulation techniques now allow the construction of tiny heat engines using a single Brownian particle [1, 2], or even electrons in a quantum dot [3], as the working medium. Thermodynamic variables characterizing these devices fluctuate strongly [4]. The framework of stochastic thermodynamics [5, 6] extends the macroscopic notions of work and heat to describe these fluctuating engines and their efficiencies. The classical results are recovered upon averaging [7]. A recent experiment studying a colloidal heat engine operating in a bacterial bath [8] led to the generalization of this framework to encompass Brownian heat engines operating in active baths [9–12].

When the probe-bath interaction can be captured by an effective temperature, the heat engine with an active bath obeys the same (average) thermodynamics and achieves the same performance as with a fictitious equilibrium bath at the same temperature [10, 13]. The mapping thus allows one to derive bounds on the performance of an active heat engine from the second law of thermodynamics. Furthermore, it provides a route how to represent the thermodynamics of complicated non-equilibrium heat baths by much simpler, effective models.

In this work, we study how far such a reduced model for the active heat engine reproduces not only the (average) thermodynamic variables but also their stochastic fluctuations. In contrast to previous computer simulations, where the active bath was assumed to provide an exponentially correlated noise [14, 15], we go one step further and consider a cyclic heat engine based on a harmonically confined colloidal particle interacting with an explicitly modeled active bath composed of interacting active Brownian particles. Our model heat engine is inspired by the bacterial heat engine of Ref. [8], and its

(average) thermodynamic performance is analyzed in a companion paper [13].

A general theoretical approach to develop low-dimensional coarse-grained models from complicated many-body systems is to integrate out degrees of freedom that are not of interest [16]. This procedure requires a faithful mathematical description of the complete experimental system to which the coarse-graining shall be applied, which might not be available in the case of a bacterial heat bath. Theoretical work often resorts to the (questionable) limit of weak bath-probe coupling [17, 18] and yields viscoelastic probe dynamics with a friction kernel and a (generally non-Gaussian [19]) noise with multiple time-scales. It leaves the practitioner somewhat puzzled with regard to its experimental implications. The following is intended to provide a remedy in this regard.

As our main result, we find that for a wide range of experimentally relevant parameter values, the probe is surprisingly well described by a harmonically confined active Ornstein-Uhlenbeck particle (AOUP) [20] with exponentially correlated Gaussian noise and without necessitating a friction renormalization. The coarse-grained effective model reproduces quantitatively the work, heat, and efficiency distributions of the simulated active heat engine, even when the noise autocorrelation function is non-exponential. The AOUP model is linear, and thus, besides providing a significant speed-up of computer simulations, it is also amenable to analytical treatment by techniques described in Ref. [4], providing explicit exact results for simple driving protocols. It thus becomes a very convenient tool for fitting and interpreting experimental data, which is particularly useful for measuring probability densities or large deviation functions, for which getting good statistics is a challenge.

The manuscript is structured as follows. In Sec. II, the full numerical model of a colloidal heat engine operating in an active bath is introduced. The statistics of the colloid's position and the noise autocorrelation function are discussed in Sec. III. As our main result, we show in Sec. IV how to use the AOUP model to reproduce the stochastic work, heat, and efficiency. We conclude in

* wiese@itp.uni-leipzig.de

† viktor.holubec@mff.cuni.cz

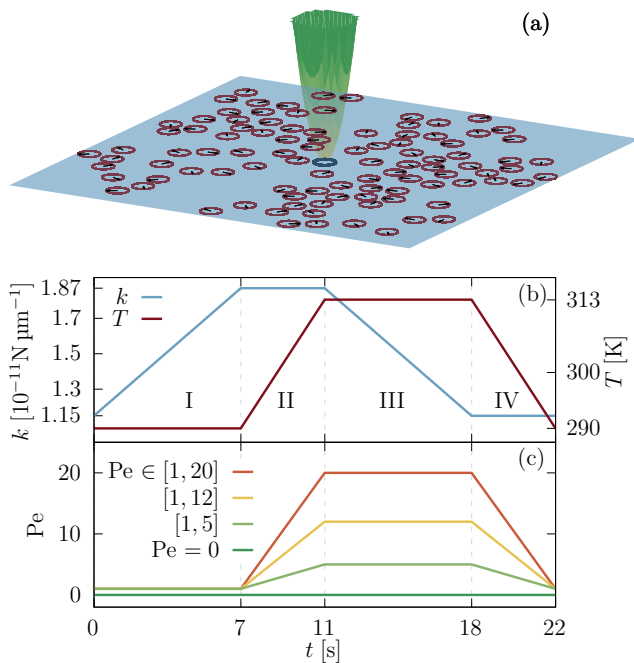


FIG. 1. Active heat engine, numerical setup, and protocols (graphics adapted from Ref. [13]). (a) Snapshot of the simulated two-dimensional setup, showing the passive tracer (blue disk), which is trapped by a parabolic potential (green) and interacts with a bath of active particles (red disks) in a solvent (blue). (b) Cycle protocols of the trap stiffness $k(t)$ and solvent temperature $T(t)$ of the colloidal Stirling engine [1]. (c) The activity of the bath particles is governed by a time-dependent Péclet number $Pe(t)$ that follows the solvent temperature.

Sec. V.

II. MODEL OF A BACTERIAL HEAT ENGINE

We study a colloidal probe particle trapped in a harmonic potential $U(\mathbf{r}) = k\mathbf{r}^2/2$ of stiffness k and diffusing in a suspension of ABPs, as sketched in Fig. 1(a). The dynamics of the probe’s position vector obeys the overdamped Langevin equation

$$\dot{\mathbf{r}} = \mu_0 \mathbf{F} - \mu_0 k \mathbf{r} + \sqrt{2D_t^0} \boldsymbol{\xi}. \quad (1)$$

As the only modification from the companion paper [13], the probe’s diameter d_0 and accordingly its mobility $\mu_0 = \mu d/d_0$ and translational diffusivity $D_t^0 = k_B T \mu_0 = D_t d/d_0$ are allowed to differ from those of the N bath ABPs. The dynamics of the latter is governed by the overdamped Langevin equations (for $i = 1, \dots, N$)

$$\begin{aligned} \dot{\mathbf{r}}_i &= \mu \mathbf{F}_i + v_a \mathbf{n}_i + \sqrt{2D_t} \boldsymbol{\xi}_i, \\ \dot{\theta}_i &= \sqrt{2D_r} \nu_i. \end{aligned} \quad (2)$$

The mutually independent unbiased normalized Gaussian white noises $\boldsymbol{\xi}$, $\boldsymbol{\xi}_i$, and ν_i model the thermal noise

of the solvent at temperature T , in which the colloid and the ABPs are suspended. Only the latter self-propel at a constant speed v_a along their orientations $\mathbf{n}_i = (\cos \theta_i, \sin \theta_i)$, while their orientation angles θ_i diffuse with rotational diffusivity D_r . As in the experiment, their motion is assumed to be unaffected by the trap potential.

The particles only interact when closer than $r_{ij} = |\mathbf{r}_i - \mathbf{r}_j| < 2^{1/3} d_{\text{eff}}$. Here, and in Eq. (3), $i = 0$ is understood to refer to the probe. For mutual interactions between ABPs, the effective diameter d_{eff} is given by the bath particle radius d , and for interactions with the probe by $d_{\text{eff}} = (d_0 + d)/2$. The repulsive interparticle forces \mathbf{F} and \mathbf{F}_i derive from an isotropic soft pair potential

$$V(r_{ij}) = 4\epsilon \left[\left(\frac{d_{\text{eff}}}{r_{ij}} \right)^6 - \left(\frac{d_{\text{eff}}}{r_{ij}} \right)^3 + \frac{1}{4} \right] \quad (3)$$

with energy scale $\epsilon \gg k_B T$.

The described setup was designed to model the colloidal heat engine in a bacterial bath previously studied in experiments [8]. As in Ref. [13], we therefore choose model parameters that mimic the experimental conditions. For micron-sized particles ($d = 1 \mu\text{m}$), the corresponding Stokes mobility is $\mu = 5 \times 10^7 \text{ s kg}^{-1}$ for water at temperature 290 K and a realistic rotational diffusivity is $D_r = 1 \text{ Hz}$, which are the values used throughout our study.

The dynamical equations are solved (iteratively) using Brownian dynamics simulations with time step $dt = 20 \mu\text{s}$ inside a square box of side length L with periodic boundary conditions. We employ a moderate bath packing fraction $\phi = N\pi d^2/4L^2 = 0.2$ and particle number $N = 10^2$ for “small” probe sizes ($d_0 < 5 \mu\text{m}$) and $N = 500$ for “larger” ones ($d_0 \geq 5 \mu\text{m}$).

Thermodynamic control parameters are the stiffness of the trap k for the probe and the swim speed v_a of ABPs. As in the experiments, T is assumed to determine the swim speed v_a . The probe particle is subjected to a cyclic driving protocol of period $t_p = 22 \text{ s}$, mimicking the Stirling cycle [1, 8, 13]. It consists of piecewise constant and linear profiles in the trap stiffness $k(t)$ and solvent temperature $T(t)$, which are modulated between $k_{\text{min}} = 1.15 \times 10^{-11} \text{ N } \mu\text{m}^{-1}$ and $k_{\text{max}} = 1.87 \times 10^{-11} \text{ N } \mu\text{m}^{-1}$ and $T_c = 290 \text{ K}$ and $T_h = 313 \text{ K}$, as depicted in Fig. 1(b). The durations of isothermal and isochoric processes are set to 7 s and 4 s, respectively, as in the experiment [8]. The ABPs’ activity $Pe(t)$ follows the solvent temperature $T(t)$ in the range $Pe \in [1, 10^2]$, as shown in Fig. 1(c). The non-dimensional Péclet number is $Pe = v_a/dD_r$. Energy is measured in units of $k_B T_c = 4.002 \text{ N } \mu\text{m}$ and observables are saved at a rate of $\Delta t = 2 \text{ ms}$, as in the experiments [8].

III. STATISTICS OF THE TRACER PARTICLE

In this section, we find a range of relative probe sizes and bath activities for which the active noise \mathbf{F} in

Eq. (1) is Gaussian and exponentially correlated, which are the conditions for coarse-graining the heat engine to the AOUP model. The dynamical equation (1) for the probe's position is linear; hence, the noise is Gaussian when the position is Gaussian distributed. In Sec. III A, we, therefore, assess the non-Gaussianity of the probe position distribution in a stationary trap potential by means of its fourth cumulant and diffusive rescaling. In Sec. III B, we study the active noise's autocorrelation function (ACF). It is found that, to a good approximation, the relevant properties of the active bath are independent of the probe's dynamics, trap stiffness, and background noise intensity. Therefore, the depicted measurements are limited to constant driving parameters $k = k_{\min}$ and $T = T_c$, corresponding to their minima in the Stirling protocol.

A. Position distribution of the probe

We consider first the effect of the relative probe size on its position distribution for fixed diameter but different values of the Péclet number of the ABPs in the bath. Since the intensity of the individual particle collisions has a finite variance, the central limit theorem implies that the probability density of the active noise intensity experienced by the probe should become Gaussian with increasing relative probe size d_0/d due to the increasing collision frequency. Due to the radial symmetry of the potential, the probability densities for x and y components of the position vector \mathbf{r} are the same.

In Fig. 2, we show the distributions $p(x)$ for the x coordinate of the probe. The color codes for the activity in the top panels (a) and (b) and the probe diameter in the bottom panels (c) and (d). At $Pe = 0$, $p(x)$ is given by the Boltzmann distribution

$$p(x) = \sqrt{\frac{k}{2\pi k_B T}} e^{-kx^2/2k_B T}. \quad (4)$$

It stays approximately Gaussian for weak activity ($Pe \lesssim 5$), while at higher activities ($Pe \geq 5$), exponential tails appear, and only the center of the distribution remains Gaussian. The Gaussian center of the distribution is due to the background thermal noise, as was also observed in the experiment [8]. The tails arise from rare “head-on collisions” of persistent active particles with the probe, which result in large displacements. In an intermediate regime, our numerical $p(x)$ can be fitted well by a superposition of Gaussian and Laplacian distributions, as proposed in Refs. [21, 22]. At the highest Pe -values considered ($Pe = 10^2$), the tails are no longer purely exponential, and the fit fails.

Rescaling the distributions by their standard deviations $\sqrt{\sigma}$ makes them collapse when they are approximately Gaussian (so-called diffusive scaling [21, 22]). Figure 2(b) shows that increasing the bath activity Pe makes the tails of $p(x)$ more non-Gaussian. The lower two panels in Fig. 2(c)-(d) show raw and scaled $p(x)$ for different

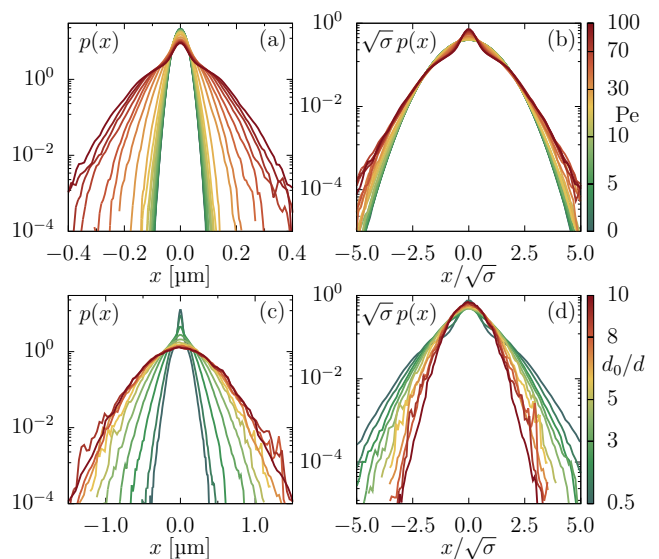


FIG. 2. Position distributions $p(x)$ for the x -coordinate of the trapped probe: (a), (b) for small probe size $d_0 = d = 1 \mu\text{m}$ and varying activity Pe (color code), showing heavy tails for higher activities compared to the normal distribution at $Pe = 0$; (c), (d) at large constant $Pe = 100$, for increasing probe diameter d_0 (color code) approaching a Gaussian shape; (b), (d) rescaling the histograms by their standard deviation $\sqrt{\sigma}$ makes them collapse in case they are Gaussian [21, 22]. Data measured at k_{\min} and T_c .

probe sizes (color code) at the highest activity $Pe = 100$. As expected, the distributions are non-Gaussian for small relative probe diameters (blue curves) and gradually become Gaussian upon increasing d_0 (red curves).

To verify our conclusion that decreasing bath activity or increasing probe size makes the active noise more Gaussian, we investigated the variance and the kurtosis of the position distribution. The mean and skewness of the distributions are zero due to symmetry. We therefore focus on the even moments in the following.

The variance $\sigma \equiv \langle \mathbf{r}^2 \rangle$ controls the average thermodynamic performance of the active heat engine, regardless of the shape of the position distribution. In Fig. 3(a), σ is represented in terms of the equivalent effective temperature $T_{\text{eff}} = k\sigma/(2k_B)$ [10, 13], which exhibits an approximately quadratic growth both in terms of probe size d_0 and activity Pe , except for the passive result ($Pe = 0$) at the bottom, for which $T_{\text{eff}} \equiv T_c$. This behavior is in accord with the theoretical expectation, $T_{\text{eff}} = T + \frac{1}{2k_B} \frac{v^2 d^2}{\mu^2 k + \mu d D_r}$, valid for the effective AOUP and ABP models [10, 13]. Generally, considering only the Gaussian center to define an effective temperature underestimates the phenomenologically correct $T_{\text{eff}} = k\sigma/(2k_B)$ and the associated work and heat, consistent with the second law [8]. As a technical remark, we note that for large activities and probe sizes, it is important to consider a bigger system with $N = 500$ ABPs and the same density to avoid finite size effects, as we ob-

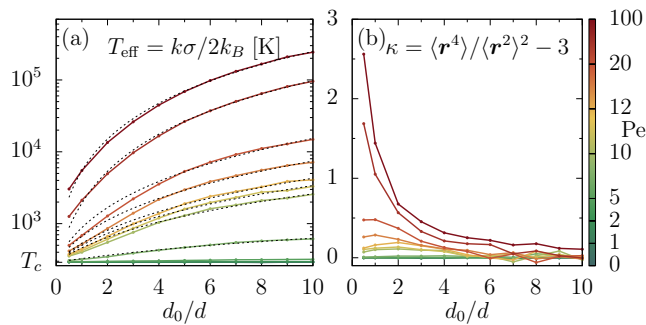


FIG. 3. Second and fourth cumulants of the position distribution $p(x)$ over the relative probe size d_0/d for different activities (color code). Dashed lines in (a) are quadratic fits. Data measured at k_{\min} and T_c .

served T_{eff} to be noticeably underestimated for $d_c \geq 5 \mu\text{m}$ and $N = 10^2$.

The excess kurtosis κ in Fig. 3(b) quantifies how much the distributions deviate from a Gaussian ($\kappa = 0$). In agreement with our conclusions from Fig. 2, we observe highly non-Gaussian effects for small probes $d_0 \approx d$ and high activities ($\text{Pe} \gtrsim 10$) when the measured kurtosis approaches $\kappa = 3$, corresponding to that for the Laplacian distribution $p(x) = e^{-|x|}/2$. An increase in probe size leads to a decline in κ , as the noise fluctuations eventually become Gaussian, in accord with the central limit theorem and literature results. Indeed, leptokurtic distributions were theoretically predicted for a 1d model with shot noise [19] and experimentally observed for tracer dynamics on cell substrates [23]. Gaussian force and position distributions were found for an underdamped model of a large, heavy probe in an active bath [24, 25].

B. Active noise autocorrelations

To identify the parameter regime where the active noise \mathbf{F} in Eq. (1) is not only Gaussian but also exponentially correlated, we sampled its ACF in our simulations at constant stiffness $k = k_{\min}$ and temperature $T = T_c$, using a sampling rate of $dt = 20 \mu\text{s}$ instead of $\Delta t = 2 \text{ms}$ as used elsewhere in the paper. We checked that the results are not visibly dependent on the trap stiffness, as it is expected since the active bath is coupled to the potential only indirectly and weakly, via the interactions with the probe particle. When analyzing experimental data, one can approximately access the ACF of \mathbf{F} by studying the autocorrelation of $\dot{\mathbf{r}} + \mu_0 k \mathbf{r}$, which is proportional to the sum of active and white noise $\mu_0 \mathbf{F} + \sqrt{2D_t^0} \boldsymbol{\xi}$. In experiments, both quantities will be integrated over a sampling time interval Δt . Furthermore, since we found the cross-correlation $\langle \mathbf{F}(t) \cdot \boldsymbol{\xi}(0) \rangle$ to be negative in our simulations [13], we expect it to also affect the ACF measured in experiments. Nevertheless, results from our simulations should be sufficiently generic to provide quanti-

tative estimates for the case of interest, namely when one can successfully model experiments with an effective AOUP. Besides, it turns out that, for the stiff traps employed in recent experiments [8], the more easily checked requirement of Gaussian noise fluctuations is much more relevant than the condition of exponential noise ACFs.

Several example ACFs for the active noise obtained from our simulations are shown in Fig. 4(a) for $d_0 = d$. The general overall trend is a speed-up of the decay with increasing activity. At high activities ($\text{Pe} \gtrsim 20$), the ACFs decay exponentially, indicated by the dashed exponential fits. The passive and low-activity ACFs exhibit a two-step decay, revealing some non-hydrodynamic short-time contributions. They are better approximated by a weighted sum of an exponential and a stretched exponential (dash-dotted lines),

$$c_1 e^{-\sqrt{t/\tau_1}} + c_2 e^{-t/\tau_2}, \quad (5)$$

with $\tau_2/\tau_1 \approx 10^2$, and $\tau_1 \approx 10^{-2} \text{s}$. The same form of the noise ACF has previously been observed in a similar system with a different interaction potential [26].

For the larger relative probe size $d_0/d = 10$ and high activities ($\text{Pe} \gtrsim 20$) in Fig. 4(b), we find the ACFs to decay more rapidly. They can be fitted by compressed exponentials

$$c e^{-(t/\tau)^\alpha} \quad (6)$$

with $\alpha > 1$, shown by the dotted lines in Fig. 4(b).

We attribute these behaviors of the ACF to different spatial configurations and degrees of clustering of the active bath particles induced by the interactions with the probe [27]. For dilute active systems below densities at which global motility-induced phase separation occurs, the mean cluster size was found to grow linearly with the swim speed of the ABPs [28, 29]. The simulation snapshots in Figs. 4(c)-(e) and the distributions of local densities in Fig. 11 in App. A indeed suggest an increased clustering of the bath ABPs around the probe, with growing activity. In the passive or low-activity regime ($\text{Pe} \lesssim 20$), when the ACF has the form of a stretched exponential, the bath in Fig. 4(c) appears fluid-like. When the bath activity is increased, the ABPs form small motility-induced clusters, mainly located close to the probe, according to Fig. 4(d), in the activity regime of the exponential active noise ACF. For the highest activity displayed in Fig. 4(e), the probe is surrounded by small clusters, which presumably induces the fast decay of the ACF.

IV. FLUCTUATIONS

Let us now turn to the fluctuating thermodynamics of the active heat engine. According to the stochastic energetics formalism established by Sekimoto [5, 30], the stochastic work and heat per cycle are obtained by splitting up the rate of change of the probe's potential energy

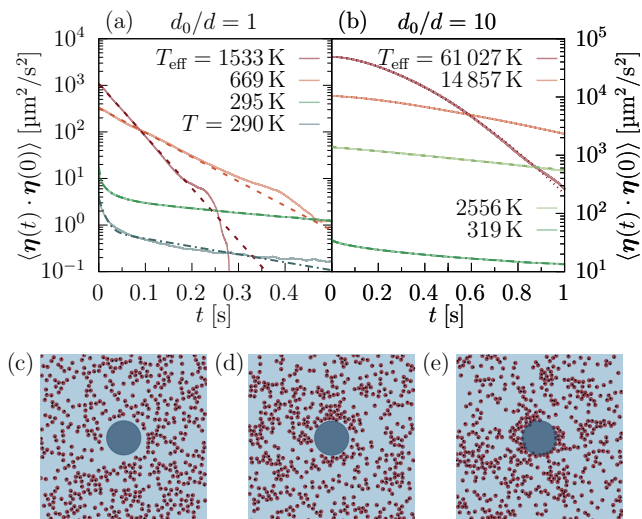


FIG. 4. Noise autocorrelation functions (ACFs) for a passive tracer in an active bath. (a),(b) show ACFs of the active component $\boldsymbol{\eta} = \mu_0 \mathbf{F}$ of the noise in Eq. (1), as measured in the simulations, and (c)-(e) the corresponding snapshots of the active bath. Identical colors in (a) and (b) correspond to the same bath activity (swim speeds of ABPs) but different effective temperatures T_{eff} and probe sizes d_0 . For $d_0 = d$ in (a), the ACF can be fitted by a weighted sum (5) of an exponential and a stretched exponential with stretching exponent 1/2 (dash-dotted lines), and at higher activities by an exponential (dashed lines), see appendix of [13] for more data. For the larger probe (b), dashed lines mark exponential fits at small and intermediate activities. For $\text{Pe} \gtrsim 20$, the decay can be fitted by the compressed exponential in Eq. (6) (dotted lines). The snapshots in the lower panels were taken for $d_0/d = 10$ and $T_{\text{eff}} = 319$ K in (c), $T_{\text{eff}} = 2556$ K in (d), and $T_{\text{eff}} = 61027$ K in (e).

according to $\dot{U} = \dot{k}r^2/2 + kr \cdot \dot{\mathbf{r}}$. The contribution to \dot{U} due to a variation of the externally controlled parameter k represents the stochastic power flowing into the system. The work performed on the engine per cycle thus reads

$$w = \frac{1}{2} \int_0^{t_p} \dot{k}(t) \mathbf{r}^2(t) dt. \quad (7)$$

The second contribution to \dot{U} is identified as the rate of heating. The stochastic heat input into the engine per cycle is then

$$q_{\text{in}} = \int_0^{t_p} k(t) \mathbf{r}(t) \cdot \dot{\mathbf{r}}(t) \Theta(\dot{\sigma}) dt. \quad (8)$$

The Heaviside step function $\Theta(\dot{\sigma})$ is nonzero when the variance grows ($\dot{\sigma} > 0$), which signals phases of systematic heating of the “medium”. These are the branches II (literal heating) and III (compression at maximum temperature and activity) of the cycle. The ratio of output work $-w$ and input heat q_{in} defines the stochastic efficiency, $\eta_s = -w/q_{\text{in}}$ [31, 32].

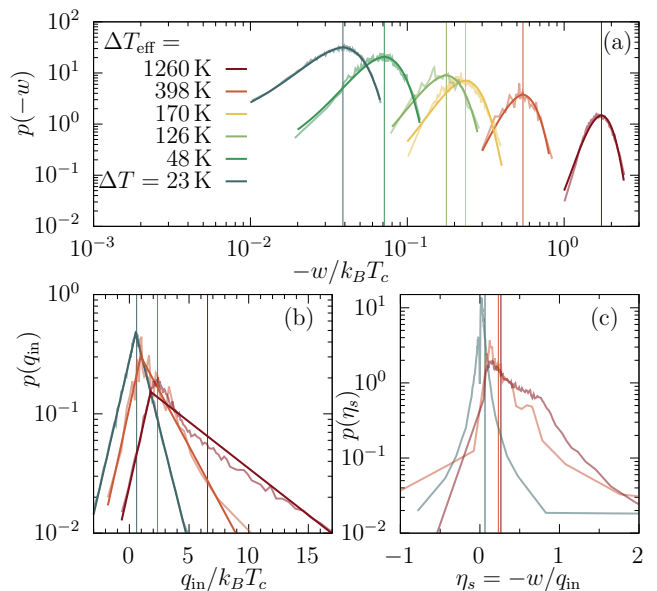


FIG. 5. Distributions of (a) stochastic output work $-w$, (b) input heat q_{in} and (c) efficiency η_s for several T_{eff} (color code) and $d_0 = d$, obtained from simulations, and their mean values (vertical lines). For each color, the more opaque solid lines in (a) and (b) represent the model fits described in the text. The work distributions $p(-w)$ have a Gaussian center and exponential tails and are (linearly) symmetric with respect to their mean. The heat distributions $p(q_{\text{in}})$ become increasingly antisymmetric with growing T_{eff} and can be approximated by exponentials with different decay rates on both sides of the maximum. (c) Distributions $p(\eta_s)$ of the stochastic efficiency.

A. Full model with active particle bath

For notational conciseness, we will distinguish the probability densities by their dependent variable in the following, using the same symbol p for all of them. The distributions $p(-w)$ of the stochastic work per cycle obtained from simulations of the active heat engine are shown as translucent lines in Fig. 5(a). Vertical lines at the mean work, $W_{\text{out}} = -\langle w \rangle$, intersect with the maxima of the distributions, showing $p(-w)$ are symmetric around $-\langle w \rangle$, which is a result of performing the cycle almost quasi-statically [4]. (That the distributions in the figure appear asymmetric is caused by the double logarithmic scale.) The distributions exhibit a Gaussian center around the mean work and exponential tails, which is underscored by fitting Gaussian-Laplacian distributions (straight opaque solid lines) to the simulation data. This shape of the work distribution is commonly reported in the literature [4, 33–36]. The Gaussian center corresponds to a large number of ‘typical trajectories’ yielding output work close to the mean value and is a universal consequence of the central limit theorem. On the other hand, the tails correspond to rare independent collisions, yielding exceptionally large or small values of work.

The distributions $p(q_{\text{in}})$ of the stochastic heat accepted by the engine per cycle obtained from the simulations are shown as translucent lines in Fig. 5(b), together with fits by asymmetric Laplacian distributions. The heat distributions have broad asymmetric tails around a Gaussian center, which is also much narrower than that of the work distributions. This indicates that work done by cyclic heat engines is a self-averaging quantity, whose Gaussian character improves with increasing cycle duration, while the heat fluctuations can remain large even for quasi-static driving [4, 37].

Figure 5(c) shows the distributions $p(\eta_s)$ of the stochastic efficiency from our simulations. The probability distributions have very heavy tails, and all of their moments diverge due to the sensitivity of the efficiency to small denominators [38]. Higher physical relevance than $p(\eta_s)$ has the large deviation function of the stochastic efficiency [31, 32, 39–41]. We decided to calculate the stochastic efficiency distributions because their complex shape poses a stern test for the validity of the mapping to the AOUP model. The classical efficiency distribution is bimodal with peaks at negative and positive η_s for zero activity, corresponding to heat engine and refrigerator modes of operation of the system [38]. With increasing activity, we find that $p(\eta_s)$ becomes unimodal with a maximum at a positive η_s .

B. Effective AOUP model

As our main results, we demonstrate in this section that numerical distributions of work, heat, and efficiency from the full model of Sec. II can be reproduced by an effective AOUP model when the active noise \mathbf{F} is Gaussian during the whole cycle and exponentially correlated during the large-activity part of the cycle.

The AOUP model is described by coupled overdamped Langevin equations for the probe position \mathbf{r} and the active noise term \mathbf{v} , which can be interpreted as the swim

speed of an active particle,

$$\begin{aligned}\dot{\mathbf{r}} &= -\mu k \mathbf{r} + \mathbf{v} + \sqrt{2D_t} \boldsymbol{\xi}_t, \\ \tau \dot{\mathbf{v}} &= -\mathbf{v} + \sqrt{2D_a} \boldsymbol{\xi}_a,\end{aligned}\quad (9)$$

where the zero-mean, unit-variance Gaussian white noises $\boldsymbol{\xi}_t$ and $\boldsymbol{\xi}_a$ represent fluctuations in an equilibrium solvent [42, 43]. The equivalent of the force exerted on the probe by the active bath in Eq. (1) is thus given by $\mathbf{F} = \mathbf{v}/\mu$, i.e., by the swim force of an effective microswimmer, a property that could hold more generally for thermodynamic interfaces in active baths [44]. After formally solving Eq. (9), one finds the velocity autocorrelation function $\langle \boldsymbol{\eta}(t) \cdot \boldsymbol{\eta}(0) \rangle = 2D_a e^{-t/\tau} / \tau$, where τ plays the role of a rotational diffusivity or persistence time of the effective microswimmer. The values of the mobility μ , trap stiffness k , and diffusivity D_t in the effective model (9) remain those of Sec. II. The active noise intensity D_a , and the persistence time τ , are determined from fits to our above simulation data for the passive tracer in the active bath.

In Sec. III, we found that the active noise ACF from the simulations is exponentially correlated for sufficiently high activity ($\text{Pe} \gtrsim 10$) for small probes ($d_0 \approx d$) [13, 26], and intermediate activity ($10 \lesssim \text{Pe} \lesssim 20$) for larger probes ($d_0 \gtrsim 5d$). We also found that sufficiently large probes experience Gaussian active noise. For the parameters used in our study, the active noise was always close to Gaussian for $d_0/d \sim 10$. To fit the AOUP model to our simulations, we thus extract the persistence time τ from the decay of the measured active noise ACF at the maximum Péclet number throughout the cycle. In the same spirit, the magnitudes of the ACFs could be used to determine also D_a , but this would require measuring the ACF for all Péclet numbers during the cycle. We therefore determined D_a by instead requiring that the mean work per cycle in the effective model equals that found in the simulations. Therefore, we used the analytical expression for the mean work W_{out} done in the considered quasi-static cycle by a heat engine based on the effective AOUP [13],

$$W_{\text{out}} = k_B(T_h - T_c) \log \frac{k_{\text{max}}}{k_{\text{min}}} + k_B(\tau \mu k_{\text{min}} + 1) [\Delta T_{\text{eff}} - (T_h - T_c)] \log \frac{k_{\text{max}}(\tau \mu k_{\text{min}} + 1)}{k_{\text{min}}(\tau \mu k_{\text{max}} + 1)}, \quad (10)$$

where the effective temperature difference [10, 13]

$$\Delta T_{\text{eff}} = T_h - T_c + \frac{D_a}{\mu k_B(\tau \mu k_{\text{min}} + 1)} \quad (11)$$

neglects the effect of a small swim speed during the cold isotherm ($T = T_c$) for the effective model [13]. The noise

intensity of the effective model can then be expressed as

$$D_a/\mu = \frac{W_{\text{out}} - k_B(T_h - T_c) \log \frac{k_{\text{max}}}{k_{\text{min}}}}{\log \frac{k_{\text{max}}}{k_{\text{min}}} - \log \frac{1 + \tau \mu k_{\text{max}}}{1 + \tau \mu k_{\text{min}}}} \quad (12)$$

where W_{out} is the average work numerically measured in the simulation.

Let us now test the ability of the effective AOUP model to predict work, heat, and efficiency fluctuations of the tracer. The bath activity Pe in the considered protocol

varies between a negligible minimum and a maximum value. Our analysis in Sec. III implies that low activity universally implies double-exponential decay of the ACF, and thus, the actual active noise cannot be exponentially correlated during the whole cycle. Nevertheless, the considered range of trap stiffnesses and mobilities implies that the relaxation time of the probe position in the harmonic trap, $(\mu_0 k)^{-1}$, is on the order of milliseconds, i.e., much shorter than the relaxation time of the active noise in a realistic parameter regime. The stiff trap thus filters out correlations in the active noise occurring at timescales longer than $(\mu_0 k)^{-1}$ from the probe dynamics. During the brief relaxation episodes in the trap, the noise ACF changes only very slowly and can thus approximately be fitted by an exponential even when it is globally non-exponential.

Indeed, Figs. 6, 7, and 8 corroborate that, for a large probe ($d_0 = 10d$), for which the active noise is Gaussian for all Pe, the distributions obtained from the effective AOUP model and the simulations agree nicely, regardless of the precise form of the ACF. This holds, in particular, for the broad heat and efficiency distributions. Deviations in the tails of the work distributions are minimal in Fig. 7 and increase as the part of the cycle during which the active noise ACF is non-exponential grows. Similarly, the probability densities nicely agree for a small probe ($d_0 = d$) and low activity in Fig. 9, where the noise ACF is approximately Gaussian with $\kappa \lesssim 0.5$. Increasing noise activity and non-Gaussianity render the agreement worse, as shown in Fig. 10, for which the ACF is exponential, but the position distribution is highly non-Gaussian.

To close this section, we note that increasing the probe diameter increases the relaxation time of its position in the harmonic trap. This means that for $d_0/d = 10$, as used in Figs. 6, 7, and 8, the cycle is perceived as effectively 10 times faster by the probe than for $d_0/d = 1$, as in Figs. 9 and 10. As a result, the cycles for $d_0/d = 10$ are no longer approximately quasi-static. Instead of symmetric work distributions [33], they, therefore, generate a long exponential tail of positive work values.

V. CONCLUSION AND OUTLOOK

We studied a numerical model of a cyclic bacterial heat engine for varying sizes of the colloidal tracer and different swim speeds of the surrounding active bath particles. We identified parameter regimes where an effective AOUP toy model exhibits the same stochastic thermodynamics as a full-fledged Brownian dynamics simulation of the engine. The most important condition is that active noise experienced by the tracer is Gaussian, which occurs for moderate bath activities when the tracer particle is several times larger than the bath particles but also for comparable particle sizes and low activities. Secondly, the noise autocorrelation function should be exponential, which occurs for intermediate activities. However, the latter requirement can be softened by using stiff traps,

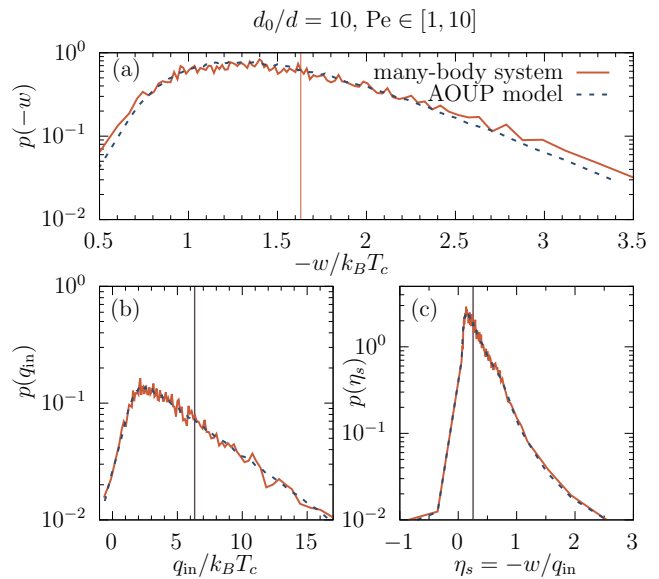


FIG. 6. Distributions of stochastic work w , heat q_{in} and efficiency η_s in the effective AOUP model (dashed lines) compared to the full model (solid lines) for a large probe size ($d_0 = 10d$). The bath activity during the cycle was varied in the interval $Pe \in [1, 10]$, or equivalently, $T_{eff} \in [296 \text{ K}, 2556 \text{ K}]$. From Figs. 2(d) and 3, it follows that the active noise is in this parameter regime almost Gaussian. From Fig. 4(b), it further follows that the noise ACF is exponential along the hot isotherm.

inducing fast relaxation of the tracer position, and filtering out the non-exponential part of the noise autocorrelation function. Such stiff traps are commonly used in current experiments with bacterial heat engines [8], making the AOUP an ideal model to reproduce or analyze the measured data. Noteworthy, we have performed a similar analysis using the active Brownian particle (ABP) model [10], which is very similar to the AOUP except that the active noise fluctuations are non-Gaussian, finding no nontrivial parameter regime where the fluctuations of the full-fledged model and the ABP model would agree.

When the mapping of the tracer dynamics in the active bath to that of the effective active Ornstein-Uhlenbeck particle works, the latter can be used to predict, with good to perfect accuracy, work, heat, and efficiency distributions or the corresponding large deviation functions, which are usually hard to measure in experiments. Besides computer simulations, for simple piecewise constant protocols, one can solve for these distributions even analytically, using the techniques described in Refs. [4, 37]. To be specific, our analysis shows that the effective models should capture the experimental results in Ref. [8] for tracers (slightly) larger than the bacteria and for bacterial swim speeds $v_a \simeq \mathcal{O}(10 \mu\text{m s}^{-1})$. Our operational approach to coarse-graining could also be useful to find effective models in other situations.

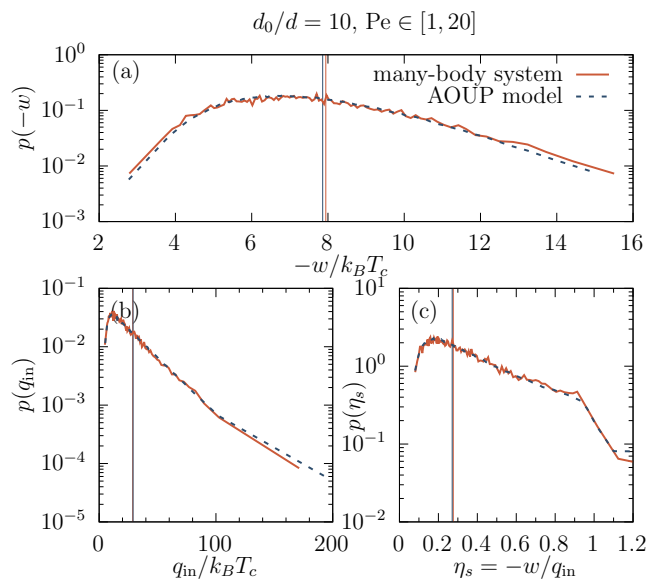


FIG. 7. As Fig. 6 but for $Pe \in [1, 20]$ and thus $T_{\text{eff}} \in [296 \text{ K}, 14857 \text{ K}]$, corresponding to Gaussian active noise and compressed exponential ACFs, as shown in Fig. 4(b).

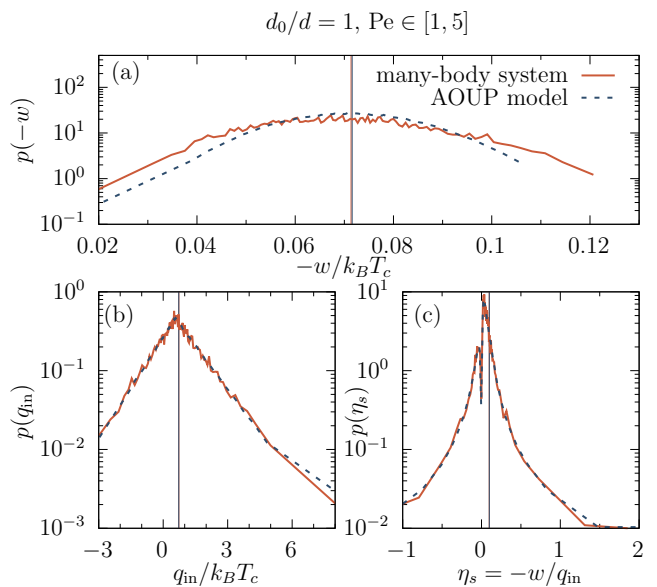


FIG. 9. As Fig. 6 but for $d_0/d = 1$, $Pe \in [1, 5]$, and thus $T_{\text{eff}} \in [293 \text{ K}, 318 \text{ K}]$, corresponding to Gaussian active noise and stretched exponential ACF, as shown in Fig. 4(a)

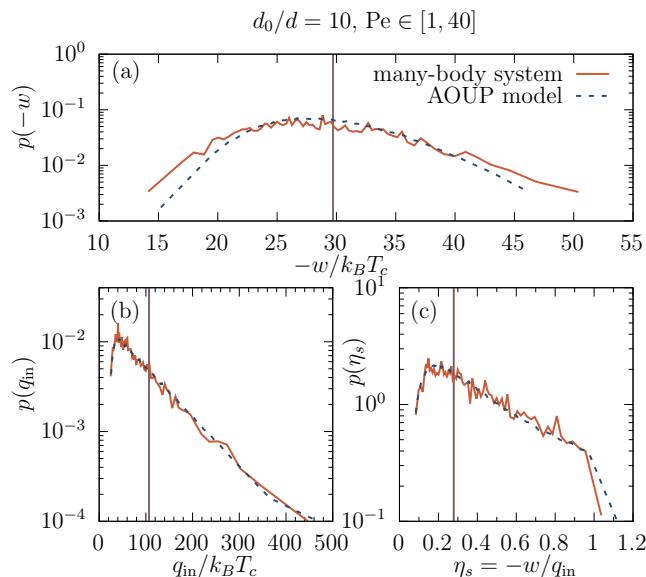


FIG. 8. As Fig. 6 but for $Pe \in [1, 40]$ and thus $T_{\text{eff}} \in [296 \text{ K}, 61027 \text{ K}]$, corresponding to Gaussian active noise and compressed exponential ACFs, as shown in Fig. 4(b).

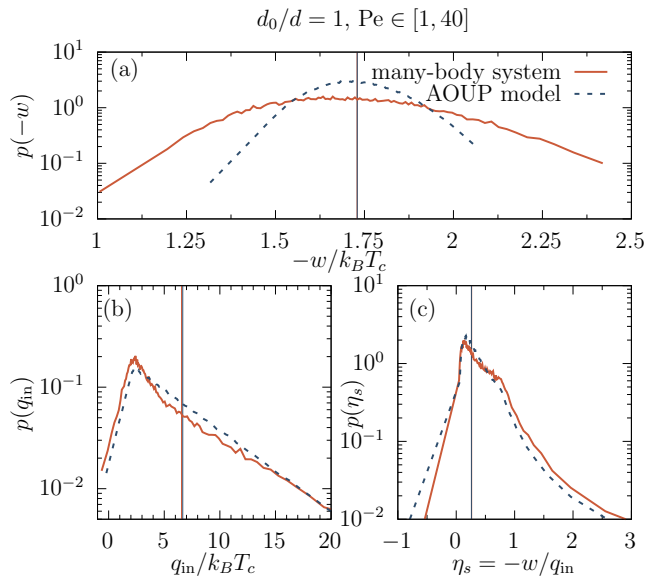


FIG. 10. As Fig. 6 but for $d_0/d = 1$, $Pe \in [1, 40]$ and thus $T_{\text{eff}} \in [293 \text{ K}, 1533 \text{ K}]$, corresponding to non-Gaussian active noise and exponential ACF, as shown in Fig. 4(a).

ACKNOWLEDGEMENTS

V.H. acknowledges the support of Charles University through project PRIMUS/22/SCI/009. K.K. acknowledges financial support from the Deutsche Forschungsgemeinschaft for computational resources.

Appendix A: Local density distributions in the active bath

To quantify the tendency of bath particles to cluster upon increasing their activity, as seen in Figs. 4(d), (e), where the clustering is additionally fostered by the presence of the probe, we analyzed the distribution of local densities in the ABP bath also without the probe parti-

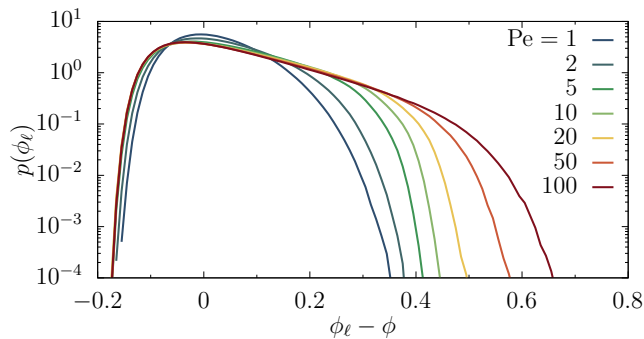


FIG. 11. The distribution $p(\phi_\ell)$ of local density ϕ_ℓ of ABPs around the global packing fraction $\phi = 0.2$ is unimodal, but broadens with increasing activity. This indicates the growing size and number of dense motility-induced particle clusters.

cle and for an increased particle number of $N = 10^4$. We used a Voronoi tessellation [45] to assign each particle i an area A_i , defined by its Voronoi cell. And we defined a local density $\phi_{\ell,i} = \pi d^2/4A_i$ for the bath ABP of diameter d . Computing a histogram for $\phi_{\ell,i}$ and averaging over 4000 particle configurations then gave the empirical distributions $p(\phi_\ell)$ shown in Fig. 11. We observe that the tails representing regions of enhanced local density $\phi_\ell > \phi$ are becoming increasingly pronounced for high activities, suggesting a growing tendency of the ABPs to cluster.

-
- [1] V. Blickle and C. Bechinger, *Nat. Phys.* **8**, 143–146 (2011).
- [2] I. A. Martínez, É. Roldán, L. Dinis, and R. A. Rica, *Soft Matter* **13**, 22–36 (2017).
- [3] M. Josefsson, A. Svilans, A. M. Burke, E. A. Hoffmann, S. Fahlvik, C. Thelander, M. Leijnse, and H. Linke, *Nat. Nanotechnol.* **13**, 920 (2018).
- [4] V. Holubec and A. Ryabov, *J. Phys. A* **55**, 013001 (2021).
- [5] K. Sekimoto, *Stochastic Energetics* (Springer Berlin Heidelberg, 2010).
- [6] U. Seifert, *Rep. Prog. Phys.* **75**, 126001 (2012).
- [7] H. B. Callen, *Thermodynamics and an Introduction to Thermostatistics* (John Wiley & Sons, 1985).
- [8] S. Krishnamurthy, S. Ghosh, D. Chatterji, R. Ganapathy, and A. K. Sood, *Nat. Phys.* **12**, 1134–1138 (2016).
- [9] A. Saha and R. Marathe, *J. Stat. Mech.* **2019**, 094012 (2019).
- [10] V. Holubec, S. Steffenoni, G. Falasco, and K. Kroy, *Phys. Rev. Res.* **2**, 043262 (2020).
- [11] É. Fodor and M. E. Cates, *Europhys. Lett.* **134**, 10003 (2021).
- [12] É. Fodor, R. L. Jack, and M. E. Cates, *Annu. Rev. Condens. Matter Phys.* **13**, 215–238 (2022).
- [13] R. Wiese, K. Kroy, and V. Holubec, *arXiv:2406.19059 [cond-mat.soft]* (2024).
- [14] A. Saha, R. Marathe, P. S. Pal, and A. M. Jayannavar, *J. Stat. Mech.* **2018**, 113203 (2018).
- [15] T. Kwon, S. Kwon, and B. J. Sung, *Soft Matter*, (2024).
- [16] T. Schilling, *Physics Reports* **972**, 1 (2022), coarse-Grained Modelling Out of Equilibrium.
- [17] S. Steffenoni, K. Kroy, and G. Falasco, *Phys. Rev. E* **94**, 062139 (2016).
- [18] D. Martin, C. Nardini, M. E. Cates, and É. Fodor, *Europhys. Lett.* **121**, 60005 (2018).
- [19] C. Di Bello, R. Majumdar, R. Marathe, R. Metzler, and E. Roldan, *arXiv:2309.13424 [cond-mat.stat-mech]* (2023).
- [20] É. Fodor, C. Nardini, M. E. Cates, J. Tailleur, P. Visco, and F. van Wijland, *Phys. Rev. Lett.* **117**, 038103 (2016).
- [21] K. C. Leptos, J. S. Guasto, J. P. Gollub, A. I. Pesci, and R. E. Goldstein, *Phys. Rev. Lett.* **103** (2009).
- [22] J.-L. Thiffeault, *Phys. Rev. E* **92** (2015).
- [23] R. Großmann, L. S. Bort, T. Moldenhawer, M. Stange, S. S. Panah, R. Metzler, and C. Beta, *Phys. Rev. Lett.* **132**, 088301 (2024).
- [24] J. Shea, G. Jung, and F. Schmid, *Soft Matter* **18**, 6965–6973 (2022).
- [25] J. Shea, G. Jung, and F. Schmid, *Soft Matter* **20**, 1767–1785 (2024).
- [26] A. Jayaram and T. Speck, *Europhys. Lett.* **143**, 17005 (2023).
- [27] J. Shea, G. Jung, and F. Schmid, *J. Phys. A: Math. Theor.* (2024).
- [28] I. Theurkauff, C. Cottin-Bizonne, J. Palacci, C. Ybert, and L. Bocquet, *Phys. Rev. Lett.* **108**, 268303 (2012).
- [29] I. Buttinoni, J. Bialké, F. Kümmel, H. Löwen, C. Bechinger, and T. Speck, *Phys. Rev. Lett.* **110**, 238301 (2013).
- [30] K. Sekimoto, *Prog. Theor. Phys. Suppl.* **130**, 17 (1998).
- [31] G. Verley, T. Willaert, C. Van den Broeck, and M. Esposito, *Phys. Rev. E* **90** (2014).
- [32] G. Verley, M. Esposito, T. Willaert, and C. Van den Broeck, *Nat. Commun.* **5** (2014).
- [33] T. Speck and U. Seifert, *Phys. Rev. E* **70** (2004).
- [34] A. Engel, *Phys. Rev. E* **80** (2009).
- [35] C. Jarzynski, *Annu. Rev. Condens. Matter Phys.* **2**, 329–351 (2011).
- [36] V. Holubec, D. Lips, A. Ryabov, P. Chvosta, and P. Maass, *Eur. Phys. J. B* **88** (2015).
- [37] V. Holubec and A. Ryabov, *Phys. Rev. Lett.* **121**, 120601 (2018).
- [38] M. Polettini, G. Verley, and M. Esposito, *Phys. Rev. Lett.* **114** (2015).
- [39] K. Proesmans, B. Cleuren, and C. Van den Broeck, *Europhys. Lett.* **109**, 20004 (2015).
- [40] I. A. Martínez, E. Roldán, L. Dinis, D. Petrov, J. M. R. Parrondo, and R. A. Rica, *Nat. Phys.* **12**, 67–70 (2015).
- [41] T. R. Gingrich, G. M. Rotskoff, S. Vaikuntanathan, and P. L. Geissler, *New J. Phys.* **16**, 102003 (2014).
- [42] D. Martin, J. O’Byrne, M. E. Cates, É. Fodor, C. Nardini, J. Tailleur, and F. van Wijland, *Phys. Rev. E* **103**, 032607 (2021).

[43] L. Dabelow and R. Eichhorn, [Front. Phys. 8 \(2021\)](#).

[44] T. Suchanek, K. Kroy, and S. A. Loos, [Phys. Rev. Lett. 131 \(2023\)](#).

[45] C. H. Rycroft, [Chaos: An Interdiscip. J. Nonlinear Sci. 19, 041111 \(2009\)](#).